Nano Research Energy

ISSN 2791-0091 CN 10-1944/O6
https://doi.org/10.26599/NRE.2026.9120219

Research Article

Precursor-solvent coordination control for defect suppression in perovskite light-emitting diodes

Eojin Yoon[1], Joo Sung Kim[1], Jung-Min Heo[1], Seung-Chul Lee[1,2], Tae-Woo Lee[1,3,4,5](✉)

[1] Department of Materials Science and Engineering, Seoul National University, 1 Gwanak-ro Gwanak-gu, Seoul 08826, Republic of Korea

[2] PEROLED Inc., Building 940, 1 Gwanak-ro, Gwanak-gu, Seoul 08826, Republic of Korea

[3] Institute of Engineering Research, Soft Foundry, Research Institute of Advanced Materials, Seoul National University, 1 Gwanak-ro, Gwanak-gu, Seoul 08826, Republic of Korea

[4] Interdisciplinary Program in Bioengineering, Seoul National University, 1 Gwanak-ro, Gwanak-gu, Seoul, Republic of Korea

[5] SN DISPLAY Co. Ltd., Building 33, 1 Gwanak-ro, Gwanak-gu, Seoul, Republic of Korea

Nano Research Energy, **Just Accepted Manuscript** • https://doi.org/10.26599/NRE.2026.9120219

https://www.sciopen.com/journal/2791-0091 on Feb. 6, 2026

Just Accepted

Table of contents

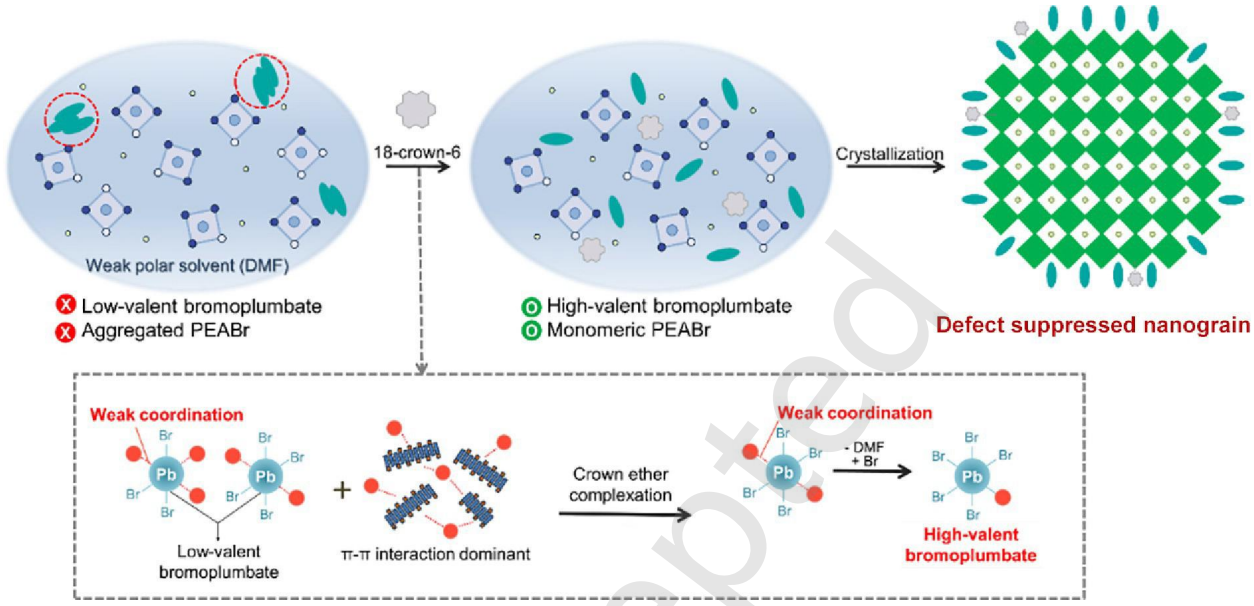

Crown ether-solvent coordination tuning in bromoplumbate precursor solutions controls defect formation in perovskite nanograins. In weakly coordinating solvent, crown ethers promote high-valent species formation, yielding defect-suppressed, highly luminescent films.

Nano Research Energy

ISSN 2791-0091 (print); 2790-8119 (online)
https://doi.org/10.26599/NRE.2026.9120219

Research Article

Precursor-solvent coordination control for defect suppression in perovskite light-emitting diodes

Eojin Yoon[1], Joo Sung Kim[1], Jung-Min Heo[1], Seung-Chul Lee[1,2], and Tae-Woo Lee[1,3,4,5] (✉)

[1] *Department of Materials Science and Engineering, Seoul National University, 1 Gwanak-ro Gwanak-gu, Seoul 08826, Republic of Korea*
[2] *PEROLED Inc., Building 940, 1 Gwanak-ro, Gwanak-gu, Seoul 08826, Republic of Korea*
[3] *Institute of Engineering Research, Soft Foundry, Research Institute of Advanced Materials, Seoul National University, 1 Gwanak-ro, Gwanak-gu, Seoul 08826, Republic of Korea*
[4] *Interdisciplinary Program in Bioengineering, Seoul National University, 1 Gwanak-ro, Gwanak-gu, Seoul, Republic of Korea*
[5] *SN DISPLAY Co. Ltd., Building 33, 1 Gwanak-ro, Gwanak-gu, Seoul, Republic of Korea*

Received: 20 November 2025 / **Revised:** 28 December 2025 / **Accepted:** 11 January 2026

ABSTRACT

Defect formation in perovskite nanograins in the polycrystalline films is governed by the solution-state coordination chemistry of halide perovskite precursor species, which have been employed to form less-defective films with large grains in solar cells. However, the coordination dynamics of bromoplumbate complexes in solution to form small grains for light-emission have been rarely studied in the context of defect suppression. In this work, we investigated the interplay between crown ether complexation and solvent coordination strength in perovskite precursor solutions, which governs the dispersion of precursor species and the formation of bromoplumbate complexes. Both crown ethers and polar aprotic solvents such as N,N-dimethylformamide (DMF) and dimethyl sulfoxide (DMSO) act as Lewis bases, competing for coordination with lead cations in the precursor solution. In weakly coordinating DMF, crown ethers can more effectively complex with precursors, shifting the coordination equilibrium toward high-valent bromoplumbate species unlike in strongly coordinating DMSO. This control yielded defect-suppressed perovskite films with nanograins with higher photoluminescence compared to those formed in strongly coordinating solvents of DMSO. These insights into bromoplumbate chemistry provide a basis for rational solvent and additive selection toward defect suppression and enhanced light-emitting performance.

KEYWORDS

perovskite light-emitting diodes, defect engineering, precursor chemistry, solvent coordination, crown ether

1 Introduction

Metal halide perovskites are regarded as ideal solid-state lighting materials due to their direct bandgap and sharp excitonic transitions, which lead to spectrally narrow emission. In addition, their intrinsic defect tolerance suppresses nonradiative recombination, enabling high photoluminescence quantum yields (PLQYs) together with narrow linewidths [1, 2]. Benefiting from these advantages, PeLEDs have achieved a remarkable steep improvement over the past decade [3–8]. Nevertheless, shallow trap states remain potential quenching centers, while vacancies can act as ion migration pathways, thereby posing a critical challenge to the operational stability of perovskite emitters [9, 10]. These considerations highlight the importance of uncovering the origins of defect formation in the films, which are closely associated with the crystallization and phase evolution of perovskite materials from the precursor solutions.

Among the various fabrication parameters, precursor solution chemistry plays a pivotal role in governing both film quality and defect management in perovskite material [11]. In solution-processed perovskites, Pb(II) ions engage in dynamic coordination with both halide anions and solvent molecules, giving rise to transient haloplumbate complexes [12]. The identity and stability of these species are dictated by the relative binding strengths of halides with solvents. Strongly coordinating polar solvents such as dimethyl sulfoxide (DMSO) tend to stabilize lead complexes with fewer halides, whereas weakly coordinating solvents e.g., gamma-butyrolactone (GBL), N,N-dimethylformamide (DMF) allow iodide-rich species such as $[PbI_6]^{4-}$ to dominate [13, 14]. These distinct solution species can be carried over into the solid state, where less-coordinated complexes may act as structural defects, degrading the electronic quality of the film [15]. In contrast, high-valent haloplumbate species with greater halide coordination are generally more favorable, as they mitigate the formation of antisite defects and halide vacancies during crystallization, thereby improving film quality and optoelectronic performance [15].

Address correspondence to Tae-Woo Lee, twlees@snu.ac.kr or taewlees@gmail.com

Meanwhile, bromide systems exhibit different precursor chemistry due to the higher donor number of Br^- (33.7 kcal·mol^{-1}) compared to I^- (28.9 kcal·mol^{-1}) [13]. Compared with iodide perovskites, bromide perovskites thus show lower solubility in common solvents and distinct solvation-phase characteristics, meaning that strategies effective for iodide systems cannot be directly applied for the bromoplumbate system [12, 16]. While iodide perovskites have been optimized mainly for photovoltaics, bromide perovskites target green light-emitting diodes, where efficient operation requires small-sized nanograins [5, 17]. Moreover, forming such nanograins requires excess spacer incorporation, which adds complexity to precursor chemistry that must be carefully addressed.

In this work, we systematically investigated the precursor coordination chemistry of formamidinium lead bromide and developed a solution-based strategy to suppress defect formation in perovskite nanograin for PeLEDs. Specifically, phenylethylammonium bromide (PEABr) was employed as a spacer ligand to restrict grain growth, and 18-crown-6 (hereafter referred to as crown ether) was introduced as a complexation additive to regulate precursor interactions. Solution-state nuclear magnetic resonance (NMR) confirmed that in weakly coordinating DMF, crown ether interacted more strongly with precursor species than in DMSO. This enhanced interaction uniformly dispersed PEABr and facilitated the formation of small, homogeneous bromoplumbate-based nanograins, while the effect was suppressed in DMSO due to stronger solvent-Pb binding. As a consequence, crown ether incorporation led to the suppression of the n = 2 phase and promoted the growth of uniform 3D perovskite nanograins. Films prepared in DMF with crown ether exhibited higher photoluminescence and longer carrier lifetimes compared to those prepared in DMSO, which we attribute to defect suppression by high-valent bromoplumbate precursors. Building on this optimized chemistry, further lattice stabilization was achieved through A-site cation engineering, yielding green-emitting diodes with a current efficiency of 45.82 cd·A^{-1} and a maximum luminance of 16,798 cd·m^{-2}.

2 Experimental

2.1 Materials

Formamidinium bromide (FABr, >99.99%), phenethylammonium bromide (PEABr, >98.0%) were purchased from Greatcell solar. Caesium bromide (CsBr), 1,4,7,10,13,16-Hexaoxacyclooctadecane (Crown ether, >99%), N,N-Dimethylformamide (DMF, anhydrous 99.8%), Dimethyl sulfoxide (DMSO, >99.9%) and chlorobenzene (CB, anhydrous 99.8%) were purchased from Sigma-Aldrich. Lead bromide ($PbBr_2$, >98.0%) was purchased from TCI. 2,2′,-2′(′1,3,5-Benzinetriyl)-tris(1-phenyl-1H-benzimidazole) (TPBi) was purchased from OSM. Lithium fluoride (LiF) was supplied by Foosung. Unless otherwise stated, all materials were used without purification.

2.2 Preparation of perovskite precursor solution

The single-cation precursor (FA) was prepared by dissolving stoichiometric ratios of FABr, $PbBr_2$, and PEABr (molar ratio FABr:$PbBr_2$:PEABr = 1:1:0.4) in the corresponding solvent at a concentration of 0.2 M. In the case of the dual-cation precursor (FACs), the composition was identical except that FABr and CsBr were mixed in a 9:1 molar ratio. The solution was stirred overnight in an N2-filled glovebox at room temperature before use.

2.3 Fabrication of PeLEDs

Prepatterned indium tin oxide (ITO) (70 nm, 25 mm × 25 mm) glasses were cleaned in acetone, and 2-propanol for 15 min, and sequentially boiled in 2-propanol for 30 min. The ITO substrates underwent UV-O treatment to attain a hydrophilic surface. We used a previously reported method to get a buffer hole-injection layer (BufHIL) that has an exciton-quenching blocking capability due to surface-enriched PFI polymer due to vertical self-organization of PEDOT:PSS (CLEVIOS P VP AI4083) and PFI copolymer to become surface-rich PFI polymer and provide a gradient work function; the solution with 1:1 weight ratio of PEDOT:PSS to PFI was spin coated to a thickness of 70 nm, then annealed at 150 °C for 15 min [4]. After annealing, the substrates were transferred to an N_2-filled glovebox for the perovskite film. Perovskite nanograin films were deposited by spin coating at 4000 rpm. In the spin-coating step, the antisolvent was dripped 6 s after the start for DMF-based solutions and 40 s after the start for DMSO-based solutions [5]. Samples were then moved to the vacuum chamber (<10^{-7} Torr) to sequentially deposit TPBi (40 nm), LiF (1 nm) and Al (100 nm). The active area of 4.3 mm^2 was defined by shadow masking during deposition of the cathode. Finally, the fabricated PeLEDs were encapsulated in a glovebox under a controlled N_2 atmosphere (O_2 < 10.0 ppm, H_2O < 1.0 ppm) by using a glass lid and UV-curable epoxy resin with 20 min of UV (365 nm) treatment.

2.4 Measurement

^{1}H NMR spectra were recorded on a high-resolution spectrometer (Bruker Advance, 600 MHz). For these measurements, the perovskite precursor solutions were prepared by dissolving the salts in deuterated solvents, DMF-d_7 or DMSO-d_6 (1 mL). All samples were handled under a nitrogen atmosphere at room temperature, and their properties were analyzed under the same conditions. Steady-state photoluminescence (PL) spectra of the perovskite films and UV–vis absorption spectra of both films and precursor solutions were obtained using a JASCO FP8500 spectrofluorometer and a V-770 UV–vis spectrophotometer. Transient PL decay profiles were measured with a FluoTime 300 spectrometer. The excitation source was a picosecond pulsed laser (LDH-P-C-405B, PicoQuant, λ = 405 nm), and detection was carried out with a hybrid photon-counting detector (PMA Hybrid 07) coupled to a time-correlated single-photon counting system (PicoHarp, PicoQuant). X-ray photoelectron spectroscopy (XPS) was performed on a Versaprobe III instrument (Ulvac-phi) using monochromatic Al Kα radiation (1486.6 eV). Atomic force microscopy (NX-10) was employed to examine surface roughness and potential, while surface morphologies were imaged by field-emission scanning electron microscopy (SUPRA 55VP). X-ray diffraction (XRD) patterns were collected using a PANalytical diffractometer with Cu Kα radiation at a scanning rate of 4 °·min^{-1}. Fourier transform infrared (FT-IR) spectra were obtained on a Nicolet iS50 spectrometer. The electroluminescence performance of the PeLED devices was characterized using a Keithley 236 source meter in combination with a Minolta CS-2000 spectroradiometer. Operational lifetime of PeLEDs was measured under constant-current conditions by simultaneously tracking brightness and applied voltage using an M760 Lifetime Analyzer (McScience) with a control computer.

3 Results and discussion

3.1 Investigation of solvent-dependent precursor-crown ether interactions

As our approach is illustrated in Fig. 1(a), we focus on precursor solution coordination chemistry to mitigate defect formation during perovskite nanograin crystallization. DMF and DMSO both produced clear and colorless solutions with complete precursor dissolution, whereas GBL, which has been widely used for iodoplumbates in solar cells, showed limited solubility and generated orange-colored solutions from disordered clusters, consistent with incomplete dissolution and the presence of low-valent polynuclear bromoplumbate species such as $[Pb_2Br_5]^{3-}$ (Fig. S1 in the Electronic Supplementary Material (ESM)) [18]. We incorporated PEABr as a spacer molecule to form small-size nanograins in polycrystalline films. Although DMF dissolves fully the precursors, its weak solvation capacity allows local stacking of PEABr, which promotes the formation of defective low-dimensional perovskites [19]. The introduction of crown ether mitigates this aggregation by stabilizing PEABr monomers and releasing Br^-, which then favors the formation of high-valent bromoplumbates. Through this sequential interaction, controlled crystallization is achieved, leading to perovskite nanograins with significantly reduced defect density with small grains for more radiative electron-hole recombination.

The interaction between crown ether and precursor components was investigated by solution-state ^{1}H NMR spectroscopy in DMF (Fig. 1(b)) and DMSO (Fig. 1(c)). In both solvents, crown ether was completely dissolved, and four types of solutions were prepared for NMR measurements: (i) PEABr, (ii) FABr, (iii) $PbBr_2$, and (iv) a complete precursor blend containing PEABr, FABr, and $PbBr_2$. The methylene protons adjacent to the crown ether ring are highly sensitive to changes in electronic environment, making them reliable indicators of host-guest complexation [19].

Upon mixing with precursor components, these protons consistently exhibited downfield shifts indicative of complex formation, with the extent of the shifts varying according to solvent and species. In DMF, the order of shifts was FABr < PEABr < $PbBr_2$, pointing to stronger interactions of crown ether with Pb^{2+}, whereas in the DMSO solution, PEABr gave the largest shift, consistent with modified interaction behavior under strong solvation. To quantitatively assess the chemical shifts depending on reaction conditions, Fig. 1(d) presents a bar graph of ^{1}H NMR shift values organized with respect to solvent and precursor components, using pristine crown ether as the reference. Overall, the use of DMF resulted in greater chemical shifts, with the representative blend exhibiting 0.1145 in DMF compared to 0.0290 in DMSO. This indicates that in weakly coordinating DMF, crown ether interacts more effectively with under-solvated Pb^{2+} ions, whereas in strongly polar DMSO, the stronger solvation of Pb^{2+} and halides diminishes its complexation effect [20]. Further evidence for crown ether interaction was obtained from the ^{1}H NMR spectra of the methylene protons from ammonium ligand in PEABr. These protons displayed upfield shifts attributable to the electron-donating effect of crown ether (Fig. S2 in the ESM). Consistent with the Pb^{2+} trend, the shifts were more pronounced in DMF than in DMSO. The PEABr-crown ether interaction involves hydrogen bonding, and its strength is sensitive to both the precursor composition and the solvent environment such as DMF or DMSO. The hydrogen-bonding strength tends to

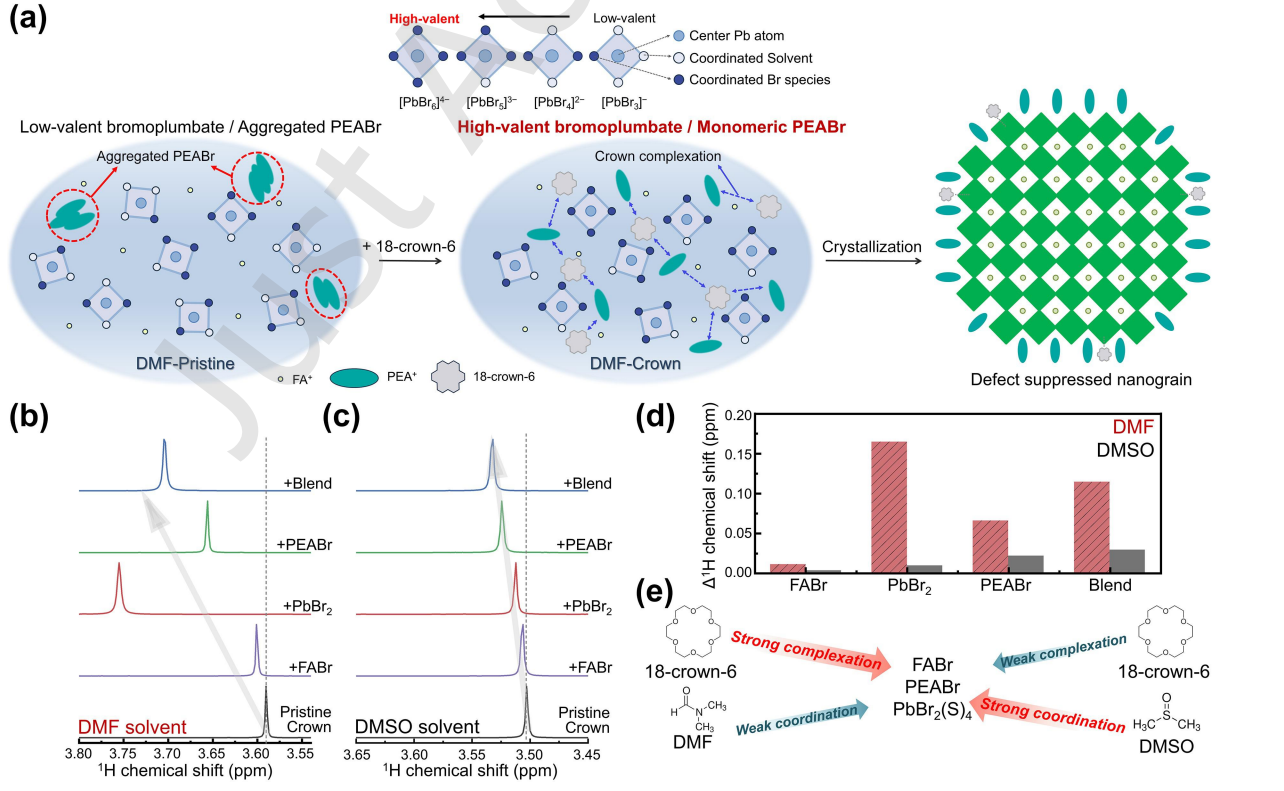

Figure 1 Investigation of solvent-dependent precursor-crown ether interactions. (a) Schematic illustration of precursor-crown ether interactions. ^{1}H NMR spectra of crown ether dissolved in DMF (b) and DMSO (c) upon addition of precursor species: Blend (PEABr+$PbBr_2$+FABr), PEABr, $PbBr_2$ and FABr. (d) Summary of quantified ^{1}H NMR shifts as a function of precursor composition. (e) Conceptual illustration of the relative complexation and coordination strength of solvent-crown ether interactions.

correlate with the magnitude of the NMR chemical shift, where larger shifts suggest stronger interactions. For example, when crown ether is in excess relative to PEABr, stronger shifts appear, consistent with enhanced hydrogen bonding [20]. Although crown ether incorporation has been tried previously in optoelectronic devices [19], our results suggests that crown ether can be more effective in weakly coordinating DMF to form small grains in polycrystalline films which will be beneficial for radiative electron-hole recombination. The competitive relationship between solvent coordination and crown ether complexation was summarized in Fig. 1(e): This shows that under the weakly coordinating DMF, crown ether binding is strengthened, whereas in the strongly coordinating DMSO, solvent-Pb coordination becomes dominant.

3.2 Colloidal characteristics of precursor solutions modulated by crown ether addition

To investigate the influence of solvent-dependent interactions between crown ether and precursor ions on the composition of bromoplumbate species, we analyzed solution-state UV–vis absorption spectra in DMF and DMSO with crown ether concentrations of 5, 10, and 20 g·L^{-1} (Figs. 2(a) and 2(b)). Notably, the higher absorption onset in DMF relative to DMSO is more consistent with a solvent-dependent shift in the coordination environment of $PbBr_4^{2-}$ species, arising from different $PbBr_4^{2-}$·solvent adduct states [21]. In DMF, the addition of crown ether induced a gradual red-shift of the absorption onset, moving from 385.83 to 390.14 nm as the crown ether concentration increased. Consistently, the gradual red-shift observed in DMF upon crown ether addition suggests the progressive formation of bromoplumbate clusters similar to $PbBr_4^{2-}$, which have been associated with absorption features in this range [21]. In contrast, no significant spectral shift was observed upon crown ether addition in DMSO. This difference in the spectral response between DMF and DMSO systems highlights the solvent-dependent nature of precursor coordination equilibria. The donor number, which represents the Lewis basicity of a solvent or anion, is conventionally defined based on its binding enthalpy to $SbCl_5$ as a reference Lewis acid, and provides a useful measure of coordinating strength [16]. Although the donor number of Br

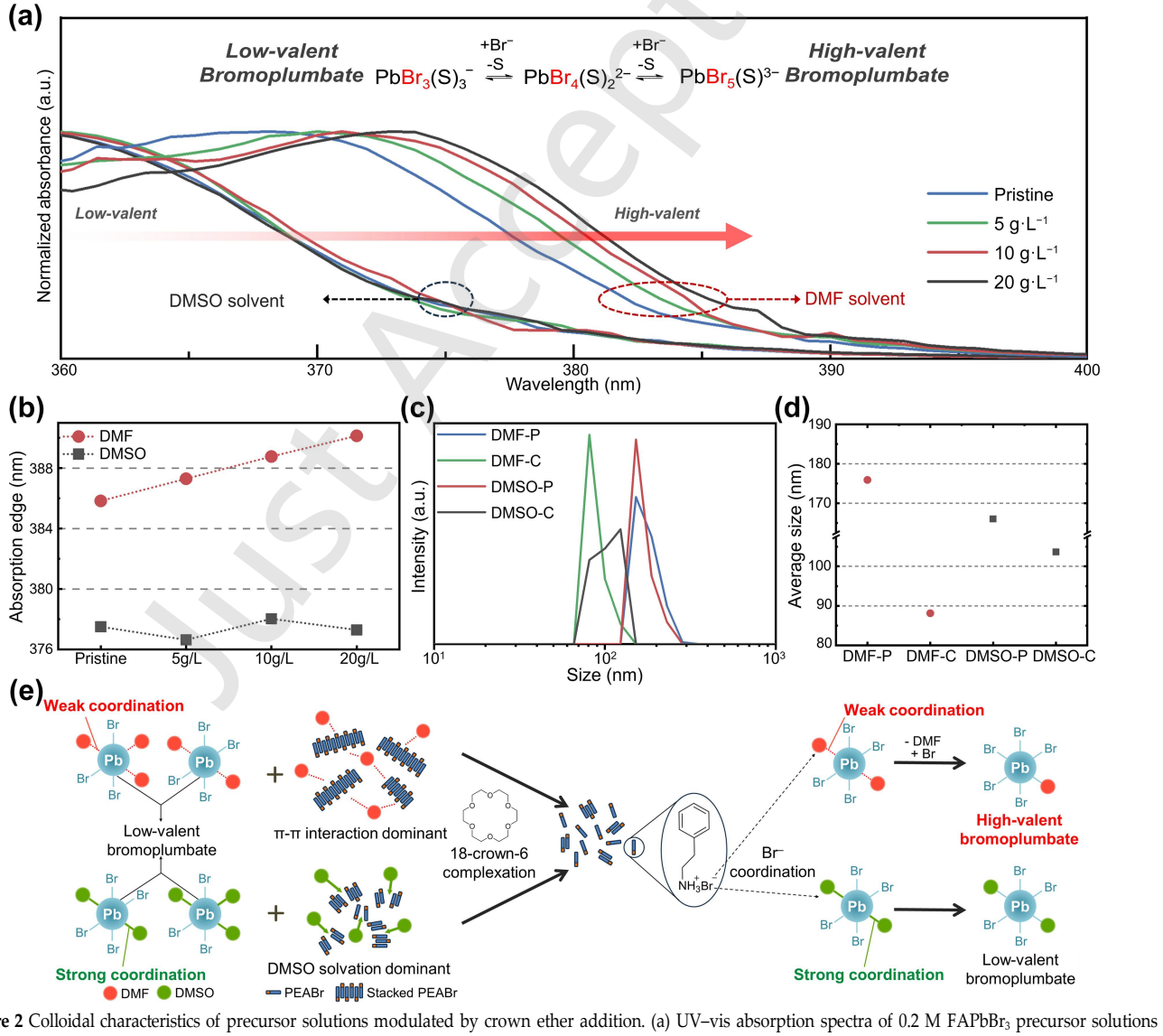

Figure 2 Colloidal characteristics of precursor solutions modulated by crown ether addition. (a) UV–vis absorption spectra of 0.2 M $FAPbBr_3$ precursor solutions containing 35 mol% PEABr with increasing crown ether content (5, 10, and 20 g·L^{-1}) in DMF, DMSO solvents. (b) Summary plot of the corresponding absorption edge shifts. (c) DLS analysis of precursor solutions described in (a), with crown ether content fixed at 5 g·L^{-1}. (d) Average precursor particle size extracted from DLS measurements. (e) Schematic illustration describing the influence of crown ether addition on bromoplumbate species.

(33.7 kcal·mol^{-1}) is higher than those of both DMF (26.6 kcal·mol^{-1}) and DMSO (29.8 kcal·mol^{-1}), the incorporation of Br^- into lead halide complexes is more effective in DMF [16]. Due to their lower binding enthalpy of DMF (26.6 kcal·mol^{-1}) and planar coordination structure, Pb-DMF complexes are more prone to halide substitution, which promotes the formation of high-valent bromoplumbate species [12]. In contrast, DMSO exhibits strong coordination to Pb^{2+} ions, facilitated not only by its high dipole moment but also by its electron-rich sulfoxide functionality, which forms a dense solvation shell around the Pb^{2+} coordination center.

Likewise, this trend is consistent with dynamic light scattering (DLS) measurements, which reveal a decrease in the hydrodynamic diameter of precursor colloids upon crown ether addition in both solvents (Fig. 2(c)). Here, the DLS results primarily capture changes in the effective size of solvated precursor colloids, which are associated with their aggregation state in solution. The samples are denoted as DMF-pristine (DMF-P) and DMSO-pristine (DMSO-P) without crown ether, and DMF-crown (DMF-C) and DMSO-crown (DMSO-C) with crown ether depending on the solvent. The larger decrease observed in DMF compared to DMSO indicates more effective suppression of precursor aggregation and enhanced dispersion upon crown ether coordination, with the hydrodynamic diameters dropping from 175.91 to 88.14 nm in DMF and from 166.04 to 103.67 nm in DMSO (Fig. 2(d)). Because DLS integrates the entire colloidal population, these changes mainly capture the mitigation of PEABr aggregation in DMF, while the red shift of the absorption onset in DMF indicates a change in lead-halide speciation toward higher-valent bromoplumbates [22].

This interpretation is aligned with iodide systems, where red shifted precursor spectra accompany a shift toward high-valent iodoplumbates and a reduction in colloid size [11]. Taken together, these results suggest a sequential mechanism in DMF as illustrated in Fig. 2(e), where weak solvation of PEABr in DMF promotes PEABr aggregation, crown ether disrupts this aggregation and releases Br^- ions, and the liberated Br subsequently replaces DMF solvent adjacent to Pb^{2+} centers, yielding high-valent bromoplumbates (Fig. 2(e)). In DMSO, the strong coordination of the solvent to Pb^{2+} impedes Br^- substitution, thereby maintaining low-valent plumbate species.

3.3 Film-level characterization of perovskite crystallographic, optical and morphological properties

To elucidate the effect of precursor coordination on film crystallinity, we conducted XRD measurements on perovskite films derived from DMF and DMSO based precursors, both in the absence and presence of crown ether (Fig. 3(a)). In pristine films, XRD patterns revealed distinct diffraction peaks of the n = 2 $PEA_2FAPb_2Br_7$ Ruddlesden-Popper (RP) phase at 4.1°, 8.2°, and 12.3°, particularly strong in DMF-P [23]. These peaks were pronounced in DMF-P, consistent with the sharp excitonic absorption near 436 nm observed in the corresponding UV-vis spectra (Fig. 3(b)). These observations indicate that the weak solvation environment of DMF for PEABr favors local PEABr aggregation, which drives the nucleation of layered RP phases [19]. In contrast, crown ether incorporation fully suppressed the RP phase formation in both solvents, as evidenced by the disappeared sharp low-angle XRD peaks and excitonic absorption bands. Steady-state PL measurements showed distinct differences among the samples. The emission peaks were observed at 523 nm for DMF-P, 521 nm for DMSO-P, and 519 nm for both crown-treated films. The red-shifted PL peak observed for DMF-P is attributed to the formation of larger 3D domains, which arises from the preferential consumption of PEABr to form the n = 2 RP phase, thereby leaving insufficient PEABr to effectively passivate the surfaces of the 3D domains with 2D layers. Accordingly, DMF-P exhibited the lowest film PLQY of 28.16%, whereas DMF-C showed the strongest emission, achieving a film PLQY of 60.31%,

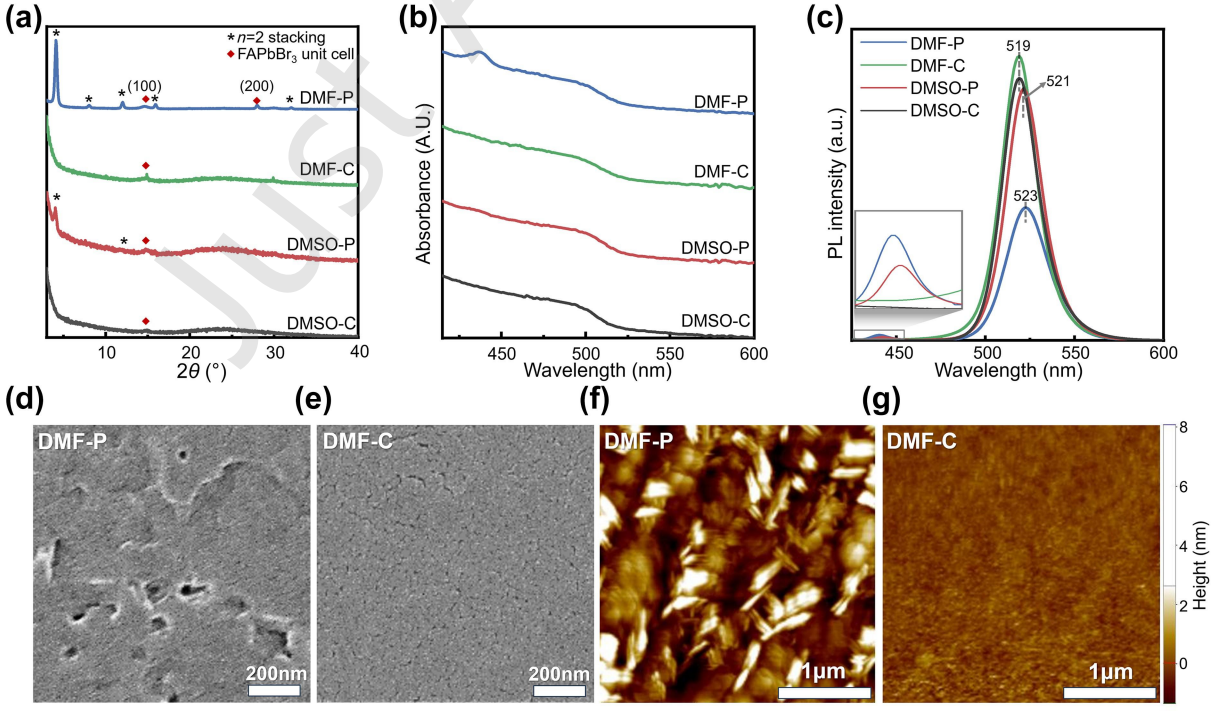

Figure 3 Film-level characterization of perovskite crystallography, optical, and morphological properties. (a) X-ray diffraction (θ–2θ) profiles, (b) UV–vis absorption spectra, and (c) steady-state PL spectra of glass/BufHIL/perovskite thin films prepared in DMF and DMSO in the presence or absence of crown ether additives. (d, e) SEM and (f, g) AFM images of perovskite thin films fabricated in DMF in the presence or absence of crown ether.

corresponding to an approximately 2.14-fold enhancement compared to DMF-P. In comparison, DMSO-P and DMSO-C exhibited film PLQYs of 53.29% and 55.65%, respectively, indicating a relatively smaller improvement upon crown treatment in the DMSO-based system. This enhancement is attributed to crown ether, which promotes the formation of high-valent bromoplumbates and ensures uniform PEABr dispersion, thereby enabling homogeneous crystallization and suppressing defect formation [11]. The morphological characterization further provided beneficial role of crown ether in DMF-based films (Figs. 3(d)–3(g), Fig. S3 in the ESM). The pristine films exhibited irregular surface coverage and numerous pinholes, most pronounced in DMF-P. In contrast, DMF-C showed compact and uniform surface morphology with reduction of root-mean-square roughness from 2.426 nm in DMF-P to 0.349 nm in DMF-C, indicating homogeneous crystallization process with crown ether.

3.4 Defect chemistry underlying enhanced PL in crown ether modified perovskite films

We further investigated the impact of crown ether incorporation on the photophysical performance of perovskite films by conducting transient PL measurements (Figs. 4(a) and 4(b)). Photon emission dynamics were recorded under 405 nm laser excitation and analyzed via tri-exponential fitting to determine the average lifetime. The individual decay components (τ_1, τ_2, and τ_3), together with their relative amplitudes and the resulting average PL decay lifetime (τ_{PL}), are summarized in Table S1 in the ESM, providing detailed photophysical parameters extracted from the tri-exponential fitting of the transient PL decay curves. DMF-P showed a markedly shorter average lifetime of 36.19 ns, whereas crown ether incorporation significantly prolonged the lifetime to 67.75 ns. DMSO-derived films exhibited a smaller enhancement, from 54.75 to 59.95 ns, suggesting that the beneficial effect of crown ether is more pronounced in DMF-based systems. DMSO-P displayed an elevated baseline at long timescales over 100 ns, which may be related to scattering effects arising from the rough surface morphology, as also seen in AFM images (Fig. S3 in the ESM). Despite this contribution, the decay dynamics are predominantly governed by sub-100 ns components that reflect defect-induced nonradiative recombination. Therefore, these results demonstrated that DMF-C reflects effective suppression of non-radiative recombination pathways. Defective nature of the perovskite films was examined via film-state XPS analysis of Pb 4f and Br 3d (Fig. 4(c), Fig. S4 in the ESM). In DMF-P, metallic Pb was detected near 141 eV, which can be attributed to uncoordinated Pb species. This suggests that the defective nature of excess RP domains adversely affects the emission properties of the films. With crown ether addition, the binding energy increased by 0.3 eV in DMF-C and 0.2 eV in DMSO-C compared with the pristine films. This binding energy shift not only evidences stronger Pb-Br bonding but also correlates with the reduced defect density and enhanced optical performance of the crown ether treated films.

Given that XPS revealed no substantial differences in Pb-Br bonding between DMF-C and DMSO-C, we investigated the effect of residual solvent behavior by performing film-state FT-IR (Figs. 4(d) and 4(e), Fig. S4 in the ESM). For this analysis, the same films were measured before and after annealing and compared with the characteristic peaks of the neat solvents. The annealing difference spectra were obtained by subtracting the FT-IR spectra recorded before annealing from those measured after thermal annealing at 70 °C for 5 min, allowing direct evaluation of annealing-induced changes associated with the removal of residual solvent species relative to their characteristic reference solvent peaks. In films processed from DMF, the characteristic peaks at ~1385 cm^{-1} (C-N stretch), ~1260–1280 cm^{-1} (C-N with $\delta(CH_3)$ coupling), and ~1100–1150 cm^{-1} (C-N stretching overtone) showed no significant variation. By contrast, DMSO-derived films displayed broad signals at 1465 cm^{-1} and ~1100–1150 cm^{-1}, indicating the presence of residual solvent species. These differences suggest that residual DMSO during annealing may lead to voids and halide vacancies [24]. These results suggest that in DMF-derived films, the weaker Pb-solvent interaction leads to almost complete evaporation of the solvent during spin-coating and do not leave residual solvent that can be detected by FT-IR and thus avoid any defect formation during annealing, leading to enhanced optical properties compared with DMSO-C.

3.5 EL characteristics of PeLEDs with different precursor chemistries

To translate the improved precursor and film properties into device-level analysis, green perovskite LEDs were fabricated under

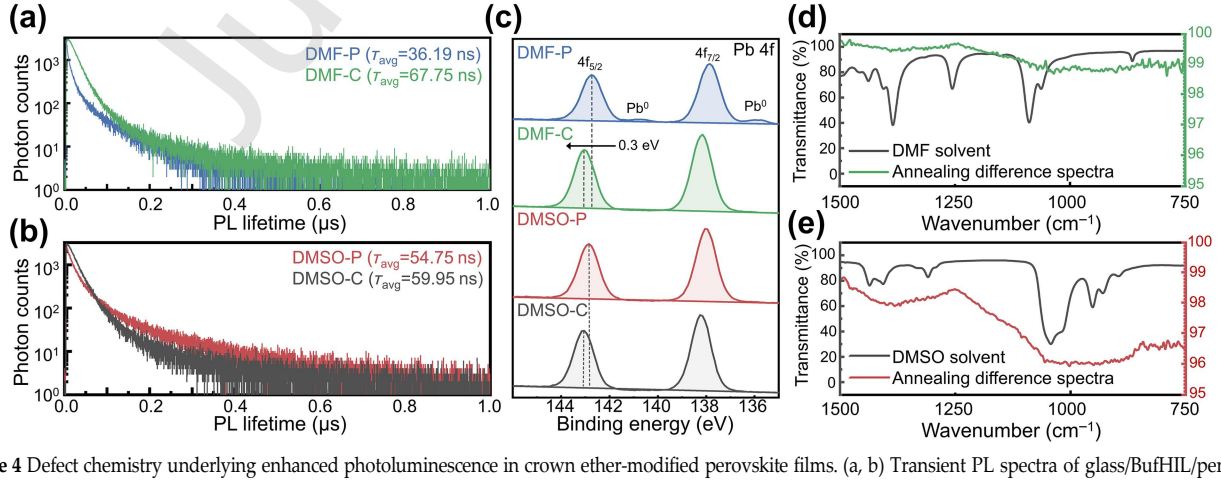

Figure 4 Defect chemistry underlying enhanced photoluminescence in crown ether-modified perovskite films. (a, b) Transient PL spectra of glass/BufHIL/perovskite thin films prepared in DMF (a) and DMSO (b) in the presence or absence of crown ether additives. (c) XPS spectra of Pb 4f core levels of Si wafer/BufHIL/perovskite thin films prepared in DMF and DMSO in the presence or absence of crown ether additives. (d, e) FT-IR spectra of comparing neat-solvent and crown ether-containing films prepared in DMF (d) and DMSO (e), measured before and after annealing to assess residual solvent. Annealing difference spectra represent the differential FT-IR signals obtained by subtracting the pre-annealed spectra from the post-annealed spectra.

different processing conditions. The schematic architecture of the device is presented in Fig. 5(a), which was designed to illustrate how solution chemistry coordination affects the device efficiencies, while the actual device structure and individual layer thicknesses are verified by the cross-sectional SEM image (Fig. S5 in the ESM). *J-V-L* and CE-*J* measurements revealed performance trends consistent with the photoluminescence behavior of the corresponding films (Figs. 5(b) and 5(c)). DMF-P, which exhibited inferior PL characteristics due to a high defect concentration, exhibited the lowest luminance and efficiency. Given that charge injection was comparable among devices, this strongly suggests that non-radiative recombination dominates in DMF-P. By contrast, the DMF-C device reached a luminance of 2,223 cd·m^{-2} and a current efficiency of 38.43 cd·A^{-1}, surpassing the performance of DMSO-C (1,781 cd·m^{-2}, 32.81 cd·A^{-1}). This improvement can be attributed to the longer carrier lifetime and the suppression of residual solvent-related defects in DMF-C films. While $FAPbBr_3$ offers a favorable bandgap for green-emitting LEDs, its structural instability can promote phase transitions that degrade optical performance [25, 26]. To mitigate the lattice instability arising from the slightly oversized tolerance factor of pure $FAPbBr_3$, we introduced A-site alloying using 10 mol% Cs (FACs), which has been shown to improve tolerance factor matching and relieve lattice strain through entropic stabilization [27]. As a result, devices based on the FACs composition exhibited stable charge injection up to 5.5 V, in contrast to pure FA-based devices that operated only up to 4.2 V. This enhanced operational stability translated into a significantly higher luminance of 16,798 cd·m^{-2}, along with markedly improved current efficiency (45.82 cd·A^{-1}) and EQE (10.66%) [28]. Beyond structural stabilization, partial Cs incorporation is also expected to suppress lattice distortion and defect-assisted nonradiative recombination, while subtly improving charge injection and interfacial energetic alignment, collectively contributing to the observed device-level performance enhancement [27, 28]. Consistent with these trends, direct operational stability measurements conducted at an initial luminance of 100 cd·m^{-2} reveal a 6.94-fold increase in the T_{50} lifetime for FACs-based devices compared to FA-only devices (Fig. S6 in the ESM). Our findings show that A-site alloying enhances stability and extends charge injection to higher voltages, thereby improving brightness. The efficiencies achieved, while promising, indicate that additional strategies beyond cationic ligand passivation could further elevate device performance such as combining precursor chemistry with anionic ligand control.

4 Conclusions

In this work, we studied the decisive role of precursor solution coordination chemistry for facilitating crystallization pathways and mitigating defect formation in perovskite nanograin films with small grain size, which can be suitable for light-emitting applications. Specifically, we analyzed how the coordination strength of solvents governs precursor complexation, tracing its influence from solution-state interactions to film formation. A comparison of DMF- and DMSO-based systems revealed that DMF, due to its weaker coordination with Pb^{2+}, enables crown ether to more effectively prevent PEABr aggregation and liberate Br^- anions when PEABr was incorporated as a spacer ligand in the precursor solutions to restrict grain growth in films. These anions readily substitute for coordinated solvent, driving the formation of high-valent bromoplumbates and suppressing defect generation. In contrast, the strong coordination of DMSO to Pb^{2+} hinders Br incorporation, thereby limiting the complexation effect of crown ether. In DMF, crown ether enabled the formation of homogeneous nanograins with suppressed RP phases and reduced defect densities, in contrast to films derived from DMSO. This improved film quality also resulted in higher luminance and current efficiency at the device level, which emphasizes the precursor chemistry as a decisive factor in device performance. Furthermore, A-site alloying provided an additional route to stabilize charge injection at higher voltages, resulting in maximum

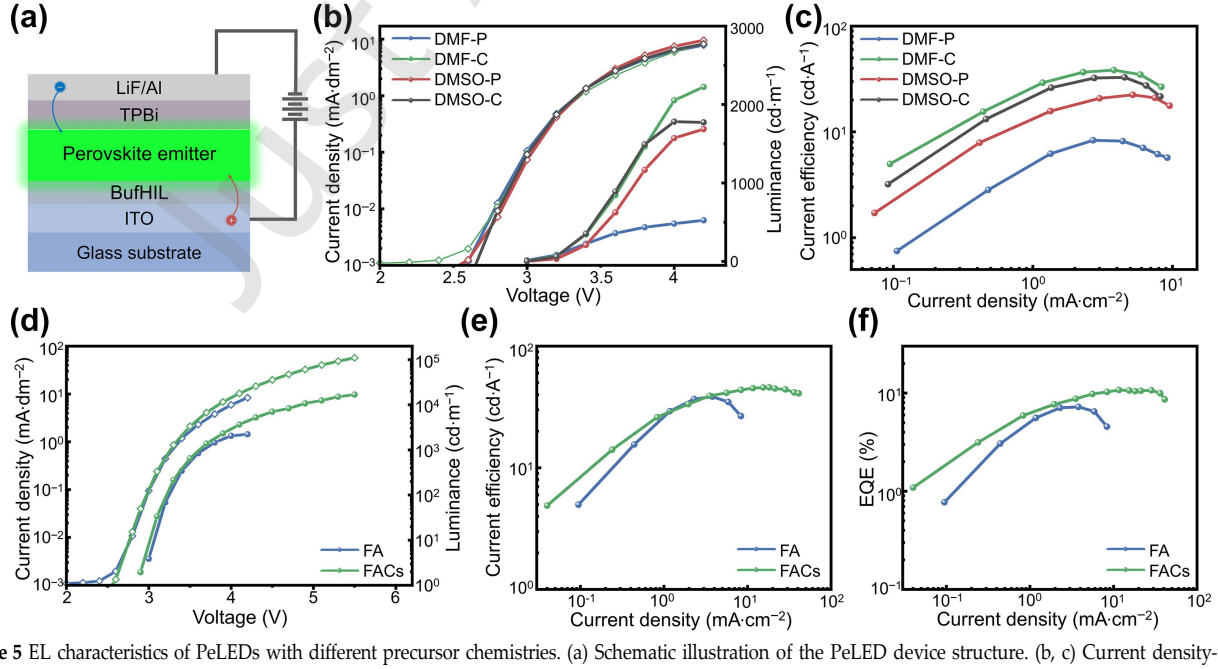

Figure 5 EL characteristics of PeLEDs with different precursor chemistries. (a) Schematic illustration of the PeLED device structure. (b, c) Current density-voltage-luminance (*J-V-L*) characteristics (b) and current efficiency versus current density (c) of PeLEDs fabricated in DMF and DMSO in the presence or absence of crown ether additives. (d–f) *J-V-L* characteristics (d), current efficiency versus current density (e), and EQE versus current density (f) of PeLEDs with additional A-site alloying (FA and FA/Cs), where FA serves as the reference.

luminance of 16,798 cd·m^{-2}. Therefore, by shedding light on the underexplored chemistry of bromoplumbates, our findings establish a foundation for rational solvent and additive selection in precursor solutions to achieve defect suppression and improved electroluminescence performance.

Acknowledgements

This work was supported by the National Research Foundation of Korea (NRF) grant funded by the Korean government (Ministry of Science, ICT & Future Planning) (RS202500560490).

Electronic Supplementary Material Supplementary material (Optical image of precursor solution, additional ^{1}H NMR results, SEM images, AFM images, FT-IR spectra, cross-SEM image and operational stability data) is available in the online version of this article at https://doi.org/10.26599/NRE.2026.9120219.

Author contribution statement

E.Y., J.S.K, J.-M.H. and T.-W.L. initiated and designed the study. E.Y. conducted the experiments. E.Y. J.S.K., J.-M.H. and S.-C.L. contributed to the analysis and interpretation of the results. T.-W.L. supervised the work. E. Y. drafted the first version of the manuscript, with assistance from T.-W.L. E.Y. and T.-W.L. jointly revised the manuscript in response to the reviewers' comments.

Declaration of conflicting interests

The authors declare no conflicting interests regarding the content of this article.

Data availability

All data needed to support the conclusions in the paper are presented in the manuscript. Additional data related to this paper may be requested from the corresponding author upon request.

References

[1] Kang, J.; Wang, L. W. High defect tolerance in lead halide perovskite $CsPbBr_3$. *J. Phys. Chem. Lett.* **2017**, *8*, 489–493.

[2] Ye, J. Z.; Byranvand, M. M.; Martínez, C. O.; Hoye, R. L. Z.; Saliba, M.; Polavarapu, L. Defect passivation in lead-halide perovskite nanocrystals and thin films: Toward efficient LEDs and solar cells. *Angew. Chem., Int. Ed.* **2021**, *60*, 21636–21660.

[3] Tan, Z. K.; Moghaddam, R. S.; Lai, M. L.; Docampo, P.; Higler, R.; Deschler, F.; Price, M.; Sadhanala, A.; Pazos, L. M.; Credgington, D. et al. Bright light-emitting diodes based on organometal halide perovskite. *Nat. Nanotechnol.* **2014**, *9*, 687–692.

[4] Kim, Y. H.; Cho, H.; Heo, J. H.; Kim, T. S.; Myoung, N.; Lee, C. L.; Im, S. H.; Lee, T. W. Multicolored organic/inorganic hybrid perovskite light-emitting diodes. *Adv. Mater.* **2015**, *27*, 1248–1254.

[5] Cho, H.; Jeong, S. H.; Park, M. H.; Kim, Y. H.; Wolf, C.; Lee, C. L.; Heo, J. H.; Sadhanala, A.; Myoung, N.; Yoo, S. et al. Overcoming the electroluminescence efficiency limitations of perovskite light-emitting diodes. *Science* **2015**, *350*, 1222–1225.

[6] Lin, K. B.; Xing, J.; Quan, L. N. ; de Arquer, F. P. G.; Gong, X. W.; Lu, J. X.; Xie, L. Q.; Zhao, W. J.; Zhang, D.; Yan, C. Z. et al. Perovskite light-emitting diodes with external quantum efficiency exceeding 20 percent. *Nature* **2018**, *562*, 245–248.

[7] Kim, J. S.; Heo, J. M.; Park, G. S.; Woo, S. J.; Cho, C.; Yun, H. J.; Kim, D. H.; Park, J.; Lee, S. C.; Park, S. H. et al. Ultra-bright, efficient and stable perovskite light-emitting diodes. *Nature* **2022**, *611*, 688–694.

[8] Peng, C. C.; Yao, H. T.; Ali, O.; Chen, W. J.; Yang, Y. G.; Huang, Z. M.; Liu, H.; Li, J. Y.; Chen, T.; Li, Z. J. et al. Weakly space-confined all-inorganic perovskites for light-emitting diodes. *Nature* **2025**, *643*, 96–103.

[9] Kim, H.; Kim, J. S.; Heo, J. M.; Pei, M. Y.; Park, I. H.; Liu, Z.; Yun, H. J.; Park, M. H.; Jeong, S. H.; Kim, Y. H. et al. Proton-transfer-induced 3D/2D hybrid perovskites suppress ion migration and reduce luminance overshoot. *Nat. Commun.* **2020**, *11*, 3378.

[10] Warby, J. H.; Wenger, B.; Ramadan, A. J.; Oliver, R. D. J.; Sansom, H. C.; Marshall, A. R.; Snaith, H. J. Revealing factors influencing the operational stability of perovskite light-emitting diodes. *ACS Nano* **2020**, *14*, 8855–8865.

[11] Kim, J.; Park, B. W.; Baek, J.; Yun, J. S.; Kwon, H. W.; Seidel, J.; Min, H.; Coelho, S.; Lim, S.; Huang, S. J. et al. Unveiling the relationship between the perovskite precursor solution and the resulting device performance. *J. Am. Chem. Soc.* **2020**, *142*, 6251–6260.

[12] Yoon, S. J.; Stamplecoskie, K. G.; Kamat, P. V. How lead halide complex chemistry dictates the composition of mixed halide perovskites. *J. Phys. Chem. Lett.* **2016**, *7*, 1368–1373.

[13] Rahimnejad, S.; Kovalenko, A.; Forés, S. M.; Aranda, C.; Guerrero, A. Coordination chemistry dictates the structural defects in lead halide perovskites. *ChemPhysChem* **2016**, *17*, 2795–2798.

[14] Radicchi, E.; Ambrosio, F.; Mosconi, E.; Alasmari, A. A.; Alasmary, F. A. S.; De Angelis, F. Combined computational and experimental investigation on the nature of hydrated iodoplumbate complexes: Insights into the dual role of water in perovskite precursor solutions. *J. Phys. Chem. B* **2020**, *124*, 11481–11490.

[15] Lee, S.; Lim, S. Y.; Kim, T.; Lee, J. H.; Kim, Y.; Ahn, H.; Hong, K. K.; Cheong, H.; Shin, H.; Wang, D. H. et al. High-valent iodoplumbate-rich perovskite precursor solution via solar illumination for reproducible power conversion efficiency. *J. Phys. Chem. Lett.* **2021**, *12*, 1676–1682.

[16] Petrov, A. A.; Ordinartsev, A. A.; Fateev, S. A.; Goodilin, E. A.; Tarasov, A. B. Solubility of hybrid halide perovskites in DMF and DMSO. *Molecules* **2021**, *26*, 7541.

[17] Jang, K. Y.; Chang, S. E.; Kim, D. H.; Yoon, E.; Lee, T. W. Nanocrystalline perovskites for bright and efficient light-emitting diodes. *Adv. Mater.* **2025**, *37*, 2415648.

[18] Fateev, S. A.; Petrov, A. A.; Khrustalev, V. N.; Dorovatovskii, P. V.; Zubavichus, Y. V.; Goodilin, E. A.; Tarasov, A. B. Solution processing of methylammonium lead iodide perovskite from γ-butyrolactone: Crystallization mediated by solvation equilibrium. *Chem. Mater.* **2018**, *30*, 5237–5244.

[19] Ban, M. Y.; Zou, Y. T.; Rivett, J. P. H.; Yang, Y. G.; Thomas, T. H.; Tan, Y. S.; Song, T.; Gao, X. Y.; Credgington, D.; Deschler, F. et al. Solution-processed perovskite light-emitting diodes with efficiency exceeding 15% through additive-controlled nanostructure tailoring. *Nat. Commun.* **2018**, *9*, 3892.

[20] Rüdiger, V.; Schneider, H. J.; Solov'ev, V. P.; Kazachenko, V. P.; Raevsky, O. A. Crown ether-ammonium complexes: Binding mechanisms and solvent effects. *Eur. J. Org. Chem.* **1999**, *1999*, 1847–1856.

[21] Dahl, J. C.; Curling, E. B.; Loipersberger, M.; Calvin, J. J.; Head-Gordon, M.; Chan, E. M.; Alivisatos, A. P. Precursor chemistry of lead bromide perovskite nanocrystals. *ACS Nano* **2024**, *18*, 22208–22219.

[22] Lian, X. M.; Chen, J. H.; Qin, M. C.; Zhang, Y. Z.; Tian, S. X.; Lu, X. H.; Wu, G.; Chen, H. Z. The second spacer cation assisted growth of a 2D perovskite film with oriented large grain for highly efficient and stable solar cells. *Angew. Chem., Int. Ed.* **2019**, *58*, 9409–9413.

[23] Yang, X. L.; Zhang, X. W.; Deng, J. X.; Chu, Z. M.; Jiang, Q.; Meng, J. H.; Wang, P. Y.; Zhang, L. Q.; Yin, Z. G.; You, J. B. Efficient green light-emitting diodes based on quasi-two-dimensional composition and phase engineered perovskite with surface passivation. *Nat. Commun.* **2018**, *9*, 570.

[24] Wang, M. R.; Fei, C. B.; Uddin, M. A.; Huang, J. S. Influence of voids on the thermal and light stability of perovskite solar cells. *Sci. Adv.* **2022**, *8*, eabo5977.

[25] McMeekin, D. P.; Sadoughi, G.; Rehman, W.; Eperon, G. E.; Saliba, M.; Hörantner, M. T.; Haghighirad, A.; Sakai, N.; Korte, L.; Rech, B. et al. A mixed-cation lead mixed-halide perovskite absorber for tandem solar cells. *Science* **2016**, *351*, 151–155.
[26] Liu, Y.; Cui, J. Y.; Du, K.; Tian, H.; He, Z. F.; Zhou, Q. H.; Yang, Z. L.; Deng, Y. Z.; Chen, D.; Zuo, X. B. et al. Efficient blue light-emitting diodes based on quantum-confined bromide perovskite nanostructures. *Nat. Photonics* **2019**, *13*, 760–764.
[27] Cho, H.; Kim, J. S.; Wolf, C.; Kim, Y. H.; Yun, H. J.; Jeong, S. H.; Sadhanala, A.; Venugopalan, V.; Choi, J. W.; Lee, C. L. et al. High-efficiency polycrystalline perovskite light-emitting diodes based on mixed cations. *ACS Nano* **2018**, *12*, 2883–2892.
[28] Saliba, M.; Matsui, T.; Domanski, K.; Seo, J. Y.; Ummadisingu, A.; Zakeeruddin, S. M.; Correa-Baena, J. P.; Tress, W. R.; Abate, A.; Hagfeldt, A. et al. Incorporation of rubidium cations into perovskite solar cells improves photovoltaic performance. *Science* **2016**, *354*, 206–209.

Eojin Yoon received his B.S. degree in Materials Science and Engineering from Seoul National University in 2019. He is currently a Ph.D. candidate in the Department of Materials Science and Engineering at Seoul National University. His current research focuses on the synthesis and surface modification of perovskite nanoparticles for perovskite LEDs as self-emissive material and photo-patterned color conversion materials for micro-LEDs.

Tae-Woo Lee received his BSc, MSc and PhD degrees in Chemical Engineering from the Korea Advanced Institute of Science and Technology (KAIST) in 1997, 1999 and 2002, respectively. He is currently a Professor in the Department of Materials Science and Engineering at Seoul National University.

Electronic Supplementary Material

Precursor-Solvent Coordination Control for Defect Suppression in Perovskite Light-Emitting Diodes

Eojin Yoon[1], Joo Sung Kim[1], Jung-Min Heo[1], Seung-Chul Lee[1,2], and Tae-Woo Lee[1,3,4,5] (✉)

[1] *Department of Materials Science and Engineering, Seoul National University, 1 Gwanak-ro Gwanak-gu, Seoul 08826, Republic of Korea*
[2] *PEROLED Inc., Building 940, 1 Gwanak-ro, Gwanak-gu, Seoul 08826, Republic of Korea*
[3] *Institute of Engineering Research, Soft Foundry, Research Institute of Advanced Materials, Seoul National University, 1 Gwanak-ro, Gwanak-gu, Seoul 08826, Republic of Korea*
[4] *Interdisciplinary Program in Bioengineering, Seoul National University, 1 Gwanak-ro, Gwanak-gu, Seoul, Republic of Korea*
[5] *SN DISPLAY Co. Ltd., Building 33, 1 Gwanak-ro, Gwanak-gu, Seoul, Republic of Korea*

Supporting information to https://doi.org/10.26599/NRE.2026.9120219

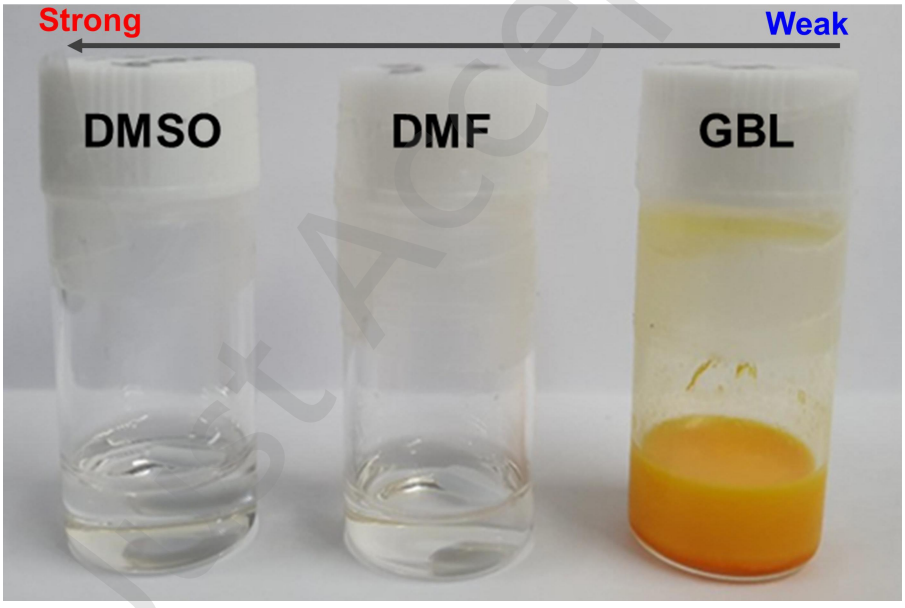

Figure S1 Optical appearance of perovskite precursor solutions dissolved in organic solvents with different polarities (DMSO, DMF and GBL)

Address correspondence to twlees@snu.ac.kr, taewlees@gmail.com

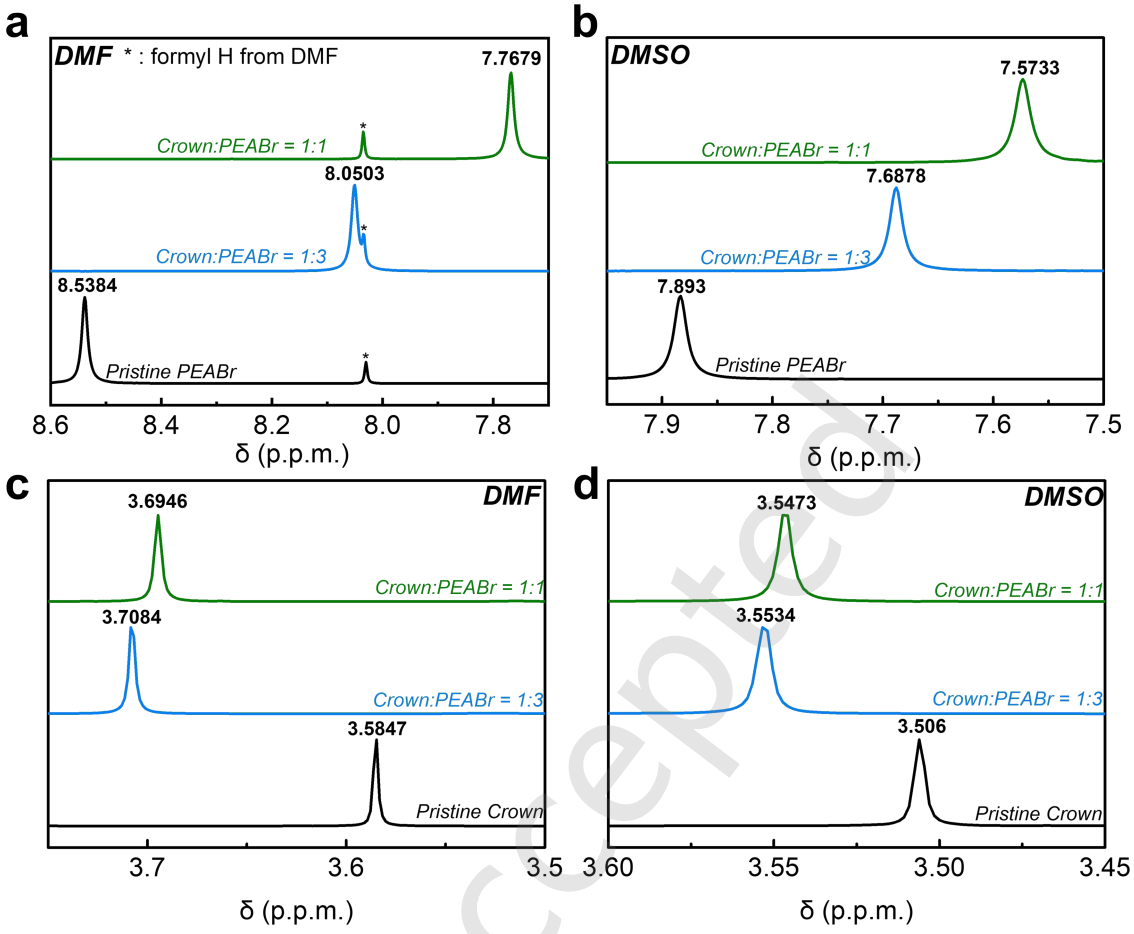

Figure S2 *^{1}H NMR chemical shifts of PEABr and crown ether in DMF and DMSO solvents. (a,b) Proton shift variations of PEABr in DMF and DMSO with different crown ether concentrations. (c,d) Proton shift variations of crown ether in DMF and DMSO with difference PEABr concentrations.*

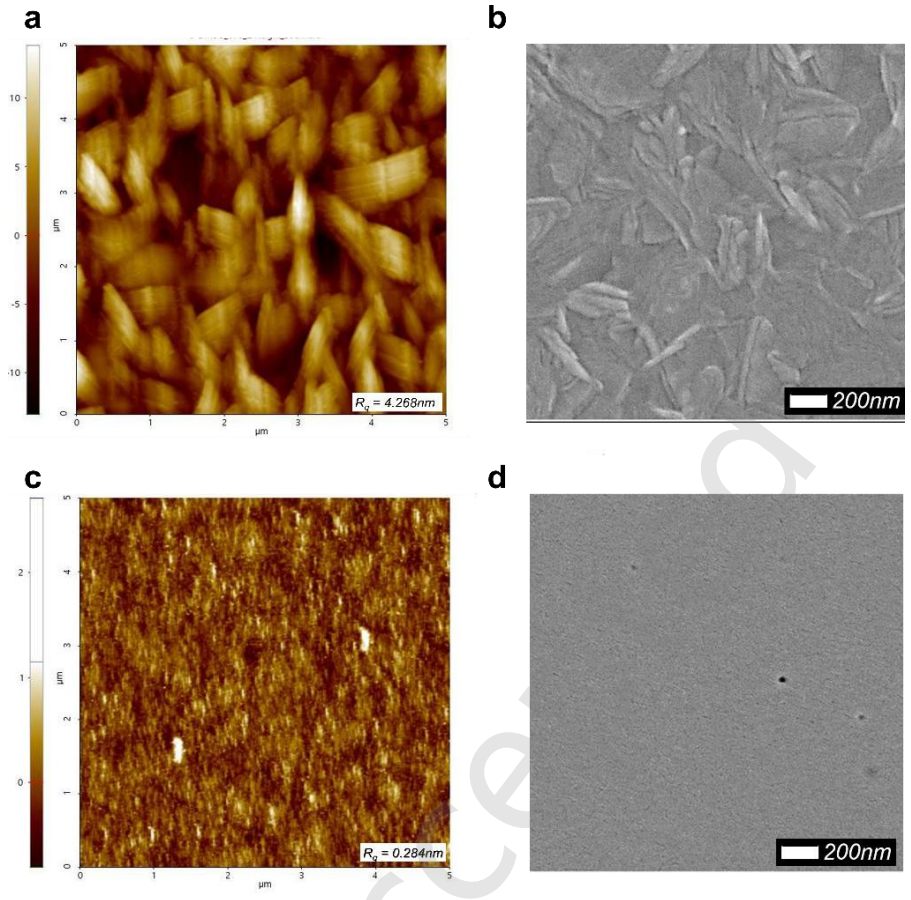

Figure S3 Surface morphology of perovskite films prepared from precursor solutions dissolved in DMSO. (a,b) Films prepared in the absence of crown ether, shown as AFM (a) and SEM (b) images. (c,d) Films prepared in the presence of crown ether, shown as AFM (c) and SEM (d) images.

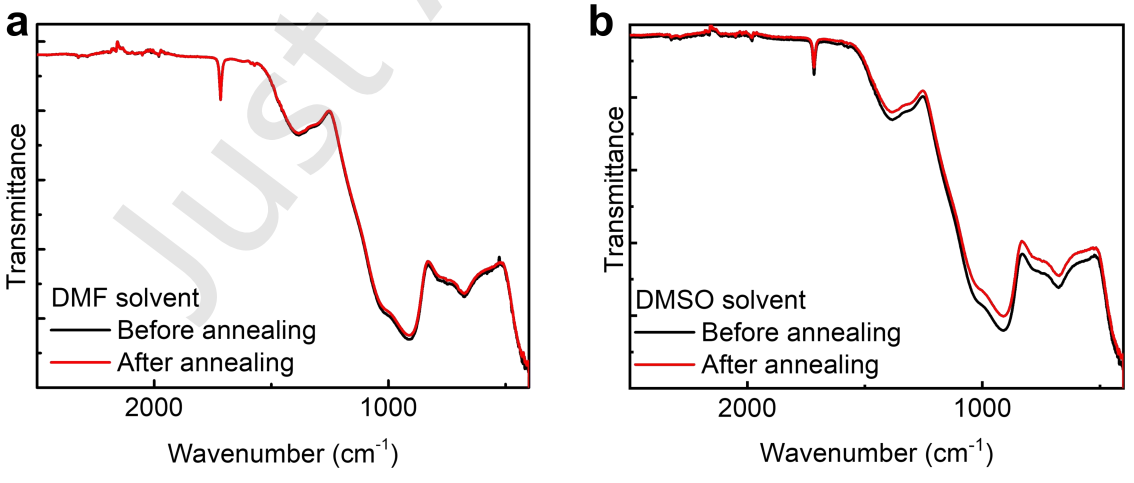

Figure S4 FT-IR spectra of perovskite films prepared by spin-coating before and after annealing process. (a) Films fabricated using DMF as a solvent (b) films fabricated using DMSO as a solvent.

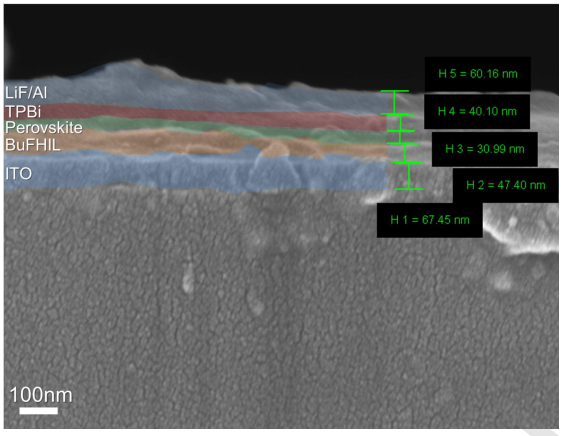

Figure S5 Cross-sectional SEM image of a representative PeLED device, showing the layer sequence of ITO/ BuFHIL/ Perovskite/ TPBi/ LiF/ Al.

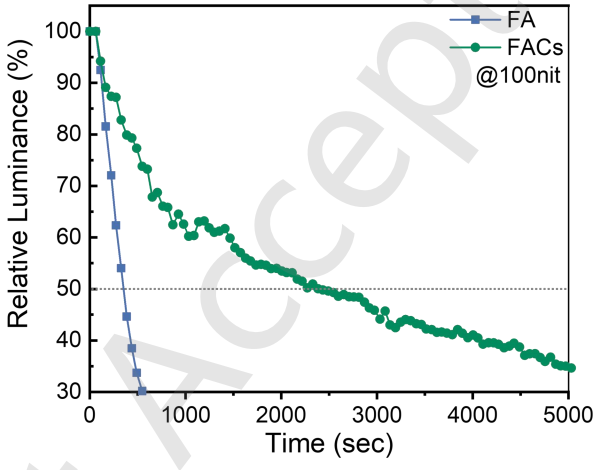

Figure S6. Operational stability of FA- and FACs-based PeLEDs measured at an initial luminance of 100 cd m^{-2}.

Table. S1. Photophysical properties of perovskite films. Average PL decay lifetime (τ_{PL}) was obtained from transient PL decay curves fitted by using a tri-exponential decay function

Sample	A_1	τ_1 (ns)	A_2	τ_2 (ns)	A_3	τ_3 (ns)	τ_{PL} (ns)
DMF P	2039.0	3.612	781.3	16.65	97.68	91.48	36.19
DMF C	3457.6	21.48	60.84	118.6	1.943	1294.0	67.75
DMSO P	1819.4	10.14	888.5	32.98	96.74	153.2	54.75
DMSO C	100.99	85.65	3265.5	21.16	3.384	831.0	59.95